Elastic Stability of Concentric Tube Robots Subject to External Loads

Junhyoung Ha*, *Member, IEEE*, Frank C. Park, *Fellow, IEEE*, and Pierre E. Dupont, *Fellow, IEEE*

***Abstract*—Concentric tube robots, which are comprised of precurved elastic tubes that are concentrically arranged, are being developed for many medical interventions. The shape of the robot is determined by the rotation and translation of the tubes relative to each other, and also by any external forces applied by the environment. As the tubes rotate and translate relative to each other, elastic potential energy caused by tube bending and twisting can accumulate; if a configuration is not locally elastically stable, then a dangerous snapping motion may occur as energy is suddenly released. External loads on the robot also influence elastic stability. In this paper, we provide a second-order sufficient condition, and also a separate necessary condition, for elastic stability. Using methods of optimal control theory, we show that these conditions apply to general concentric tube robot designs subject to arbitrary conservative external loads. They can be used to assess the stability of candidate robot configurations. Our results are validated via comparison with other known stability criteria, and their utility is demonstrated by an application to stable path planning.**

***Index Terms*—Concentric tube robot, continuum robot, elastic stability, optimal control.**

I. Introduction

CONCENTRIC tube robots are lightweight and slender and can assume complex-shaped curves simply by rotating and translating the concentric tubes relative to each other (see Fig. 1). Because the tip position and orientation can be directly guided and controlled along prescribed paths, concentric tube robots have been regarded with great promise as a surgical device for minimally invasive surgery.

Currently, these robots are being developed for procedures throughout the body. In neurosurgery, for example, designs have been developed to access and remove skull base tumors [1] as well as to perform intraventricular procedures [2]. Lung procedures are also an area of interest since bronchoscopes are limited in how deeply they can navigate into the lungs [3]–[5].

Manuscript received April 10, 2015; revised September 22, 2015; accepted September 23, 2015. Date of publication September 29, 2015; date of current version May 18, 2016. This work was supported by the National Institutes of Health under Grant R01HL124020. The work of J. Ha and F. C. Park was supported in part by the SNU BMRR Center (DAPA-UD130070ID), SNU-IAMD, BK21+, and MI Technology Innovation Program (10048320). *Asterisk indicates corresponding author*.

*J. Ha is with the Department of Cardiovascular Surgery, Boston Children's Hospital, Harvard Medical School, Boston, MA 02115 USA (e-mail: hjhdog1@gmail.com).

F. C. Park is with the School of Mechanical Engineering, Seoul National University.

P. E. Dupont is with the Department of Cardiovascular Surgery, Boston Children's Hospital, Harvard Medical School.

Color versions of one or more of the figures in this paper are available online at http://ieeexplore.ieee.org.

Digital Object Identifier 10.1109/TBME.2015.2483560

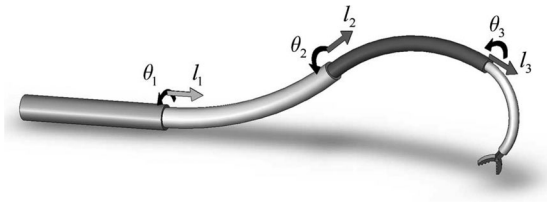

Fig. 1. Concentric tube robot consisting of four tubes.

Robotic catheters are being tested as a means of converting procedures currently performed via open surgery into beating-heart interventions [6]–[9].

In designing robots for these procedures, tubes with higher precurvatures offer better maneuverability. As tube precurvature and length increase, however, instabilities can arise [10]–[12]. Elastic potential energy stored during bending and twisting of the individual tubes can be suddenly released at certain configurations, creating dangerous snapping motions.

From a mechanics perspective, such snapping occurs when a configuration of the robot has a nearby configuration with lower energy, implying that the current configuration is not a stable equilibrium. For this reason, an understanding of local stability, in particular an efficient and reliable method for quantitatively evaluating local stability, is important in practical applications involving concentric tube robots.

For example, the design of a concentric tube robot can be cast as a problem of finding a set of design parameters that satisfies local stability over a given range of configurations, or maximizes local stability at the most unstable configuration. In sampling-based path planning algorithms such as those based on the rapidly exploring random tree (RRT) [13], a local stability criterion can be used to define the feasible configuration space. The local stability criterion can also be used for online safety checking during real-time control, to avoid such snapping configurations.

It is also important to understand and predict the effect of external loads on robot stability. A wide range of loading scenarios are possible during medical interventions. For example, concentric tube robots can be employed as steerable needles following 3-D curves through solid tissue. In these situations, loads will consist of tip cutting forces and torques as well as distributed forces and torques from the tissue along the inserted length. If a steerable needle is designed to follow a particular path through tissue, but the tissue forces are not considered, the robot may behave stably when operating in free space, but become unstable during actual insertion and cause the needle to veer off course. Since tissue properties are hard to

estimate, methods to predict robust stability would clearly be of value.

When introduced into a body cavity such as the heart, the inserted portions can operate as a robot performing such tasks as manipulating tissue and deploying devices. In these scenarios, forces and torques are generated at the robot tip. Furthermore, if the robot presses against tissue along its length, this generates distributed loads on the robot. These forces and torques can generate sudden motions. If the tip is grasping tissue delicate tissue, e.g., a heart valve leaflet, an unstable motion occurs, it could tear off the leaflet. Achieving robust stability can be important in such tissue manipulation tasks.

Existing results on the elastic stability analysis of concentric tube robots are either limited to planar tubes of constant precurvature, do not consider external loads, or otherwise require significant computation. The notion of elastic instabilities was first introduced in [11] and [12]. A global stability condition for planar tube pairs with constant precurvatures was presented in [10]; here, an analytic stability condition for measuring the stability of a tube pair based on the notion of an s-curve was developed. For robots comprised of more than two tubes, a multidimensional generalization of the s-curve was developed in [14] to determine both local and global stability.

For robots with nonconstant tube precurvatures, an analogous stability condition based on the s-curve is presented in [15]: global stability was determined from the existence of positive solutions to a certain initial value problem, and an optimal design problem to maximize global stability was also formulated and solved. An analytic stability condition for tube pairs with constant precurvatures and straight transmission lengths is presented in [16], together with an implicit method to design a globally stable robot with more than two tubes.

In summary, existing works on elastic stability assume planar and constant precurvatures [10], or those with straight transmission lengths [16]. The multidimensional s-curve approach in [14] is based on the global shape of the s-curve, which requires significant offline computations whenever the tube parameters or transmission lengths are changed. None of the prior works consider external loads in their stability analysis.

This paper presents an energy-based local stability condition for a concentric tube robot in the presence of conservative external loads, including distributed forces and torques along the tubes as well as concentrated forces and torques at the tip. While point loads applied along the length are not explicitly included, they can be closely approximated using distributed loads. Mathematical conditions for local stability are derived through a variational approach based on optimal control theory. Our results are applicable to robots comprised of any number of tubes. Furthermore, tube precurvature and stiffness can be arbitrary functions of arc length. The computations involved in evaluating local elastic stability consist simply of solving a matrix initial value problem together with the evaluation of determinants for numerical integration.

This paper is organized as follows. Section II presents the definitions and notation behind our concentric tube robot model. Section II introduces the optimality conditions from control theory that we apply to evaluating robot elastic stability. The elastostatic kinematic model is derived in a form suitable for stability analysis in Section IV, and the question of determining local elastic stability is then formulated as an optimal control problem in Section V. Numerical experiments relating our stability conditions to prior results are presented in Section VI, including tube pair examples with various external loads, and a path planning example involving a three-tube robot.

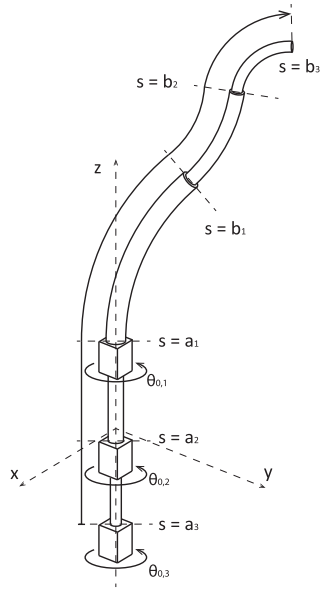

Fig. 2. Concentric tube robot with n tubes.

II. Concentric Tube Robot Modeling

The shape of the concentric tube robot is determined by external loading, the initial shape, and the stiffness of each tube, as well as the kinematic inputs including the base rotation and translation of each tube [10], [12], [17], [18]. To extend these models for stability analysis, a concise set of definitions and properties is presented here.

Consider the tubes are concentrically combined as depicted in Fig. 2. The kinematic inputs are the base rotations and the translations of the tubes about and along z-axis of the world coordinate frame. Let $\theta_{0,i}$ and a_i denote the base rotation and the translation of ith tube, and s denotes the arc-length parameter of the robot, of which the initial value is a_n and the final value is b_n.

The material coordinate frame $R_i(s) \in SO(3)$ is then defined as a body frame rigidly attached on the infinitesimal length of material of tube i at s. Its z-axis is tangentially aligned to the tube's central axis. Then, the curvature vector of tube i

$$u_i(s) = \left[u_{i,x}(s)\ u_{i,y}(s)\ u_{i,z}(s) \right]^T \in \mathbb{R}^3 \tag{1}$$

can be computed by

$$[u_i(s)] = R_i(s)^T \dot{R}_i(s) \tag{2}$$

where $[r]$ denotes the skew-symmetric representation of $r = [r_1\ r_2\ r_3]^T \in \mathbb{R}^3$ given by

$$[r] = \begin{bmatrix} 0 & -r_3 & r_2 \\ r_3 & 0 & -r_1 \\ -r_2 & r_1 & 0 \end{bmatrix} \in \mathbb{R}^{3\times 3}. \tag{3}$$

The precurvature vector of tube i, $\hat{u}_i(s) \in \mathbb{R}^3$, is defined as the initial curvature of tube i when the tube is not subject to any external loads due to the interactions between other tubes or the environment.

Since the z-axes of the material coordinate frames $R_i(s)$ of all the tubes are aligned tangentially to the backbone curve, they can be expressed with a reference coordinate frame, $R(s)$, and relative rotation angles of the tubes about the z-axis, $\theta_i(s)$, i.e.,

$$R_i(s) = R(s)R_z(\theta_i(s)) \tag{4}$$

where

$$R_z(\beta) = \begin{bmatrix} \cos\beta & -\sin\beta & 0 \\ \sin\beta & \cos\beta & 0 \\ 0 & 0 & 1 \end{bmatrix} \in \mathbb{R}^{2\times 2}. \tag{5}$$

Note that any arbitrary choice of the reference frame $R(s)$ is possible as long as its z-axis is tangentially aligned to the tube's central axis. We have chosen a Bishop frame [19] as the reference frame. Note that $\dot{\theta}_i$ represents the mechanical twisting of tube i in this case. The Bishop frame $R(s)$ and the backbone curve $p(s) \in \mathbb{R}^3$ are then given by

$$\dot{R}(s) = R(s)\left[(u_x, u_y, 0)\right] \tag{6}$$

$$\dot{p}(s) = R(s)\hat{e}_z \tag{7}$$

where $u_x(s), u_y(s) \in \mathbb{R}$ are the backbone bending curvatures, and $\hat{e}_z$ is the unit vector in the z-direction, i.e., $\hat{e}_z = [0\ 0\ 1]^T$. The initial value of $R(s)$ is chosen to be an identity matrix, i.e., $R(a_n) = I$.

Additional properties that determine the shape of the combined tubes are the bending stiffness and the torsional stiffness of each of the tubes along the length. Let $K_i(s) \in \mathbb{R}^{3\times 3}$ denote the stiffness matrix of tube i at s. Since the cross section of each tube is an annulus, the bending moment about x-axis and y-axis are the same. The stiffness matrix $K_i(s)$ is then given by

$$K_i(s) = \begin{bmatrix} k_{i,xy}(s) & 0 & 0 \\ 0 & k_{i,xy}(s) & 0 \\ 0 & 0 & k_{i,z}(s) \end{bmatrix} \tag{8}$$

where $k_{i,xy}(s)$ is the bending stiffness and $k_{i,z}(s)$ is the torsional stiffness.

As shown in Fig. 2, tube i does not exist over the entire arc-length interval $[a_n, b_n]$, but only in the interval $s \in [a_i, b_i]$. For convenience, let us introduce an equivalent model by imagining virtual tubes at the tips and the bases of the actual tubes.

Fig. 3 shows an example of the equivalent model using virtual tubes. At the proximal end, virtual tubes have zero curvature and infinite bending and torsional stiffness, while those at the tips have zero curvature, zero bending stiffness, and arbitrary positive torsional stiffness. The stiffnesses and precurvatures at the proximal end are chosen to keep the backbone curve straight and to keep the bending and the tube torsion to be zero, while the bending stiffnesses and the precurvatures at the distal end are chosen to make the virtual tubes flexible enough not to distort the backbone curve of the original model. Note that the internal axial torque on the cross section of each virtual tube at the distal end is zero based on both the boundary condition and these values, and the resulting torsions of the virtual tubes are uniquely determined to be zero as long as the torsional stiffnesses for the virtual tube, $k_{i,z}$, are chosen to be nonzero. Since the potential energy of the virtual tubes is zero at each equilibrium configuration, elastic instability, which is caused by the sudden release of the elastic potential energy, is not affected by the virtual tubes.

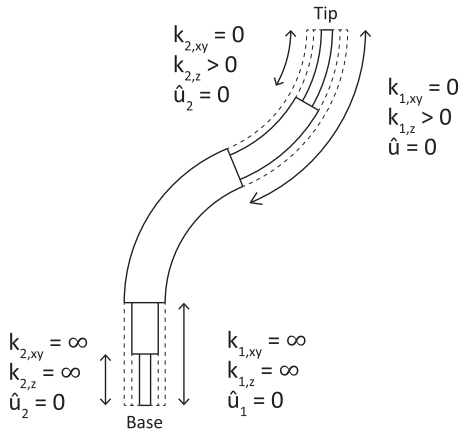

Fig. 3. Equivalent tube model.

III. Formulation of the Analogous Optimal Control Problem

The kinematics and local stability conditions to be presented in this paper are derived based on optimal control theory. We thus begin with some preliminaries on the first- and second-order conditions for optimal control.

Consider an n-dimensional state variable $x = x(s) \in \mathbb{R}^n$ and m-dimensional control variable $u = u(s) \in \mathbb{R}^m$ defined in an interval $s \in [a, b]$, which satisfy

$$\dot{x} = f(x, u, s) \tag{9}$$

$$x(a) = x_0 \tag{10}$$

where $x(b)$ is free and $\dot{x}$ denotes dx/ds. We consider the following optimal control problem:

$$\min_{u(s)\in U} \left\{ J = \int_a^b g(x, u, s)ds + h(x(b)) \right\}. \tag{11}$$

Let J_λ denote the augmented objective functional of the form

$$J_\lambda = \int_a^b \left[H(x, u, s, \lambda) - \lambda^T \dot{x} \right] ds + h(x(b)) \tag{12}$$

where

$$H(x,u,s,\lambda) = g(x,u,s) + \lambda^T f(x,u,s) \tag{13}$$

and λ is the Lagrange multiplier for the state equation (9). Assume that the first and second variations of (12) exist. The first-order necessary condition for optimal control is then given by

$$\delta J_\lambda|_{u^*}(\xi) = 0 \tag{14}$$

for all admissible state-control perturbation pairs (η, ξ) at (x^*, u^*), i.e.,

$$\dot{\eta} = \left.\frac{\partial f}{\partial x}\right|_{u^*} \eta + \left.\frac{\partial f}{\partial u}\right|_{u^*} \xi. \tag{15}$$

The solution of these equations for concentric tube robots yields the elastostatic kinematic model as derived in Section IV. To investigate stability, second-order conditions must be considered as described below.

A stationary solution (x^*, u^*) that satisfies (14) is a weak local minimum if (x^*, u^*) minimizes J over the neighborhoods of (x^*, u^*). Note that a strong local minimum is defined as a minimizer of J over (x, u) in which x is a neighborhood of x^*, while u is not necessarily a neighborhood of u^* [20]–[22].

One of the second-order necessary conditions for a weak local minimum is given by the strengthened Legendre–Clebsch condition [21], [22]:

$$\frac{\partial^2 H}{\partial u^2}(x,u,\lambda,s) \succ 0 \tag{16}$$

for given (x, u, λ) and for all $s \in [a, b]$, where $\succ$ denotes matrix positive definiteness. For the class of problems in which the strengthened Legendre–Clebsch condition is satisfied, a sufficient condition and a necessary condition for a weak local minimum are given in [22], respectively, by

$$\delta^2 J_\lambda\big|_{u^*}(\xi) > 0 \tag{17}$$

and

$$\delta^2 J_\lambda\big|_{u^*}(\xi) \geq 0. \tag{18}$$

for all admissible nonzero perturbations (η, ξ).

When the strengthened Legendre–Clebsch condition is satisfied, the Jacobi condition provides an efficient way to check if the second-order conditions (17), (18) are satisfied [22], [23]. Consider the following second variation evaluated at a stationary solution (x^*, λ^*, u^*):

$$\delta^2 J_\lambda = \frac{1}{2}\int_a^b \begin{bmatrix}\eta^T & \xi^T\end{bmatrix} \begin{bmatrix} A & B \\ B^T & C \end{bmatrix} \begin{bmatrix}\eta \\ \xi\end{bmatrix} ds + \frac{1}{2}\eta_f^T D \eta_f \tag{19}$$

where the matrices $A(s), B(s), C(s)$, and D are given by

$$A = \frac{\partial^2 H}{\partial x^2}^*, \quad B = \frac{\partial^2 H}{\partial x \partial u}^*$$
$$C = \frac{\partial^2 H}{\partial u^2}^*, \quad D = \frac{\partial^2 h}{\partial x^2}^* \tag{20}$$

and $\eta_f = \eta(b_n)$. The starred variables denote that the variables are evaluated at the stationary solution (x^*, λ^*, u^*). Here, $\eta(s)$ and $\xi(s)$ are the perturbations in the state and input, respectively, satisfying the linear state equation

$$\dot{\eta} = \frac{\partial f}{\partial x}^* \eta + \frac{\partial f}{\partial u}^* \xi \tag{21}$$

with the boundary condition

$$\eta(a) = 0. \tag{22}$$

At this stage, we assume that the optimal control u^* is continuous. Then, the Jacobi condition is given as follows.

1) Consider a linear system

$$\begin{bmatrix}\dot{\eta} \\ \dot{v}\end{bmatrix} = P \begin{bmatrix}\eta \\ v\end{bmatrix} \tag{23}$$

with a boundary condition

$$v(b) = D\eta(b) \tag{24}$$

where P is defined as

$$P = \begin{bmatrix} P_1 & -P_2 \\ -P_0 & -P_1^T \end{bmatrix} \tag{25}$$

with

$$P_0 = A - BC^{-1}B^T$$
$$P_1 = \frac{\partial f}{\partial x}^* - \frac{\partial f}{\partial u}^* C^{-1} B^T$$
$$P_2 = \frac{\partial f}{\partial u}^* C^{-1} \frac{\partial f}{\partial u}^{*T} \tag{26}$$

and $A(s), B(s), C(s)$, and D are given in (20). This linear system has no nonzero solution (η, v) on $s \in [a, b]$ such that $\eta(c) = 0$ for some c in $[a, b)$. In other words, this says that there exists no point c in $[a, b)$ *conjugate* to b.

When the strengthened Legendre–Clebsch condition is satisfied, the Jacobi condition is equivalent to the second-order sufficient condition (17). If the Jacobi condition is modified to allow the conjugate point c at a, it becomes equivalent to the necessary condition (18) [22].

These standard conditions must be adapted to accommodate discontinuities in curvature for analyzing the stability of concentric tube robots. These adaptations are described in Section V after first deriving the kinematic model below based on first-order optimality conditions.

IV. Elastostatic Kinematic Model

Following the formulation above, energy methods can be used to derive the elastostatic kinematics of concentric tube robots subject to distributed loads over the length and concentrated loads at the tip. While prior researchers have considered energy-based derivations without external loads [18] and nonenergy-based derivations with external loads [17], [24], the formulation derived in this section differs from prior formulations in the representation of external loads and cross-sectional internal moments.

Consider a concentric tube robot with n tubes in the absence of any external loads. The potential energy of the system is then given by the sum of the elastic potential energies of each of the tubes. The potential energy functional is then given by

$$J = \int_{a_n}^{b_n} \sum_{i=1}^{n} \frac{1}{2} \left(u_i(s) - \hat{u}_i(s)\right)^T K_i(s) \left(u_i(s) - \hat{u}_i(s)\right) ds. \tag{27}$$

Since the tubes are concentric, the xy curvatures of the tubes are identical to the backbone bending curvature expressed in different material coordinate frames. In order to reduce the number of variables, the bending curvatures of the tubes are expressed as a single variable $u_{xy}(s) \in \mathbb{R}^2$, which is the Bishop frame representation of the xy curvature of the backbone curve. Let $\theta_i(s) \in \mathbb{R}$ denote the rotation of tube i along the arclength, i.e.,

$$\dot{\theta}_i(s) = u_{i,z}(s) \tag{28}$$

where the upper dot represents the derivative taken with respect to the arclength parameter s, and $\theta_i(a)$ is given as a kinematic input. The bending curvature of tube i is then expressed as

$$u_{i,xy}(s) = R_z(\theta_i(s))\big|_{xy}^T u_{xy}(s) \in \mathbb{R}^2 \tag{29}$$

where

$$R_z(\beta)\big|_{xy} = \begin{bmatrix} \cos\beta & -\sin\beta \\ \sin\beta & \cos\beta \end{bmatrix} \in \mathbb{R}^{2\times 2}, \tag{30}$$

$$u_{i,xy}(s) = \begin{bmatrix} u_{i,x}(s) \\ u_{i,y}(s) \end{bmatrix} \in \mathbb{R}^2. \tag{31}$$

Substituting u_{xy} into (27) yields

$$J = \int_a^b g(u_{xy}(s), \theta(s), \dot{\theta}(s)) ds \tag{32}$$

where

$$\theta(s) = \left[\theta_1(s) \ \cdots \ \theta_n(s)\right]^T \in \mathbb{R}^n \tag{33}$$

$$g(u_{xy}, \theta, \dot{\theta}) = \sum_{i=1}^{n} \frac{1}{2} \Big\{ k_{i,xy} \| \ R_z(\theta_i)\big|_{xy}^T u_{xy} - \hat{u}_{i,xy} \|^2 + \ k_{i,z} (\dot{\theta}_i - \hat{u}_{i,z})^2 \Big\}. \tag{34}$$

The potential energy J in the above equation is a functional of $\dot{\theta}_i(s)$ as well as $u_{xy}(s), \theta_i(s)$, which results in a standard calculus of variation problem. The unloaded kinematics is then obtained by applying the Euler–Lagrange equation to (32).

Let us now assume that conservative forces are applied as the external loads. Then, there exists a total potential energy, including the elastic potential energy of the tubes and the potential energy by the external forces, of the form

$$J = \int_{a_n}^{b_n} g(u_{xy}, \theta, u_z) + w(p, R, \theta, s) ds + W(p(b_n), R(b_n), \theta(b_n), b_n) \tag{35}$$

where $u_z(s) = [u_{1,z}(s) \ \cdots \ u_{n,z}(s)]^T \in \mathbb{R}^n$, $p(s) \in \mathbb{R}^3$ is the backbone curve, and $R(s) \in \mathbb{R}^{3\times 3}$ is the Bishop frame along the arc-length; these satisfy

$$\dot{p}(s) = R\hat{e}_z \tag{36}$$

$$\dot{R}(s) = R\left[(u_x, u_y, 0)\right]. \tag{37}$$

The term $w(p(s), R(s), \theta(s), s)$ is the potential density function of the distributed loads at $s \in [a, b]$, and $W(p(b_n), R(b_n), \theta(b_n), b_n)$ is the potential energy function of the concentrated load applied to the tip. Intuitively, the tubes are considered to be subject to the reaction forces from an environment whose potential energy is $\int_{a_n}^{b_n} w \, ds + W$. Then, the total potential energy of the system including the tubes and the environment is given by J. Solving for the backbone curve, consisting of the state variables $x(s) = (p(s), R(s), \theta(s))$, that minimizes elastic potential energy (35) can be interpreted as an optimal control problem in which $u(s) = (u_{xy}(s), u_z(s))$ comprise the input variables. Note that $R(s)$ is constrained to be a rotation matrix by (37) as long as the initial frame $R(a_n)$ is a rotation matrix, even though the constraints for a rotation matrix, i.e., $R^T R = I$ and $\det R = 1$, are not explicitly applied throughout the paper. The first variation of (35) should be zero; this yields the well-known first-order necessary condition for optimal control:

$$\dot{x} = \frac{\partial H}{\partial \lambda}, \ \dot{\lambda} = -\frac{\partial H}{\partial x}, \ \frac{\partial H}{\partial u} = 0 \tag{38}$$

with boundary conditions

$$\begin{aligned} &x(a_n) \ \text{ (given as kinematic inputs)} \\ &\lambda(b_n) = \frac{\partial W}{\partial x}(b_n) \end{aligned} \tag{39}$$

where the Hamiltonian H is defined as

$$\begin{aligned} H = \frac{1}{2} \sum_{i=1}^{n} \{ & k_{i,xy} \| R_z^T(\theta_i) u_{xy} - \hat{u}_{i,xy} \|^2 \\ & + k_{i,z} (\dot{\theta}_i - \hat{u}_{i,z})^2 \} + w(p, R, s) \\ & + \lambda_p^T R\hat{e}_z + \mathrm{Tr}(\lambda_R^T R[(u_x, u_y, 0)]) + \lambda_\theta^T u_z. \end{aligned} \tag{40}$$

Here, $(\lambda_p(s), \lambda_R(s), \lambda_\theta(s)) \in \mathbb{R}^3 \times \mathbb{R}^{3\times 3} \times \mathbb{R}^n$, and $\mathrm{Tr}(\cdot)$ denotes the trace operator. Note that each component of λ_R is a Lagrangian multiplier for each corresponding component of R. The trace operator is used to represent the sum of the componentwise multiplication between λ_R and $R[(u_x, u_y, 0)]$.

The elastostatic kinematics of the concentric tube robot subject to conservative loads is then obtained from the first-order condition (38). Substituting the Hamiltonian (40) into (38) yields the following differential equations:

$$\begin{aligned} &\dot{p} = R\hat{e}_z, \ \dot{R} = R\left[(u_x, u_y, 0)\right], \ \dot{\theta}_i = u_{i,z} \\ &\dot{\lambda}_p = -\frac{\partial w}{\partial p} \\ &\dot{\lambda}_R = -\frac{\partial w}{\partial R} - \lambda_p \hat{e}_z^T + \lambda_R[(u_x, u_y, 0)] \\ &\dot{\lambda}_{\theta_i} = -\frac{\partial w}{\partial \theta_i} + k_{i,xy} u_{xy}^T \frac{dR_z(\theta_i)}{d\theta_i} \hat{u}_{i,xy}. \end{aligned} \tag{41}$$

Here, u_{xy} and $u_{i,z}$ are given by

$$u_{xy} = \frac{-\begin{bmatrix} Tr(\lambda_R^T R[\hat{e}_x]) \\ Tr(\lambda_R^T R[\hat{e}_y]) \end{bmatrix} + \sum_{i=1}^{n} k_{i,xy} R_z(\theta_i) \begin{bmatrix} \hat{u}_{i,x} \\ \hat{u}_{i,y} \end{bmatrix}}{\sum_{i=1}^{n} k_{i,xy}}$$

$$u_{i,z} = -\lambda_{\theta_i}/k_{i,z} \tag{42}$$

where $\hat{e}_x = [1\ 0\ 0]^T$, $\hat{e}_y = [0\ 1\ 0]^T$ and $\hat{e}_z = [0\ 0\ 1]^T$. The boundary conditions are given by

$$p(a_n) = [0\ 0\ a_n]^T,\ R(a_n) = I,\ \theta(a_n) = \theta_{\text{base}},$$
$$\lambda_p(b_n) = \frac{\partial W}{\partial p},\ \lambda_R(b_n) = \frac{\partial W}{\partial R},\ \lambda_\theta(b_n) = \frac{\partial W}{\partial \theta}. \tag{43}$$

For convenience, the partial derivatives $\frac{\partial W}{\partial R}$ and $\frac{\partial w}{\partial R}$ are defined to be $R^{3\times 3}$ matrices, whose components are the partial derivatives with respect to the corresponding components of R. $\frac{\partial W}{\partial p}$ and $\frac{\partial W}{\partial \theta}$ are column vectors in $\mathbb{R}^3$ and in $\mathbb{R}^n$, respectively. Note that the partial derivatives in these definitions are transposed from the conventional scalar-by-column vector or scalar-by-matrix derivatives so that the number of transposes used in the differential equations (41) is reduced.

The Lagrange multipliers λ_p, λ_R, and λ_θ in the equations are physically interpreted as the (negative) generalized forces applied to the generalized coordinates p, R, and θ. Note that $-\lambda_p$ and the ith component of $-\lambda_\theta$ are, respectively, the linear force and the z-directional moment of the ith tube on the cross section of the robot. The variable $-\lambda_R$ also represents the x, y moments on the cross section of the robot.

More familiar representations of the x, y moments are obtained by projecting the generalized force $-\lambda_R$ onto the tangent space of the rotation group $SO(3)$. We adopt the following exponential local coordinate representation for a rotation matrix about R_0:

$$R = R_0 \exp([w]) \tag{44}$$

where $w = [w_x\ \ w_y\ \ w_z]^T \in \mathbb{R}^3$ is the local coordinate variable [25]. Unit velocities along the x- and y-directions of the local coordinates yield the tangent vectors of the rotation matrix, whose components are given by

$$t_x = R_0\,[\hat{e}_x] \in \mathbb{R}^{3\times 3} \tag{45}$$
$$t_y = R_0[\hat{e}_y] \in \mathbb{R}^{3\times 3}. \tag{46}$$

To express m_x in terms of λ_R, consider an infinitesimal displacement in w_x, δw_x. The work done by this displacement is given by

$$\delta W_x = m_x \delta w_x = Tr(-\lambda_R^T t_x \delta w_x) \tag{47}$$

where the last term with the trace operator represents the inner product of the generalized force, $-\lambda_R$, and the infinitesimal displacement in the generalized coordinate, $t_x \delta w_x$. The subscript x in the above equation can be replaced with y or z for the y or z moment. The x, y moments on the cross section are then given by

$$m_x = -Tr(\lambda_R^T R_0[\hat{e}_x]) \tag{48}$$
$$m_y = -Tr(\lambda_R^T R_0[\hat{e}_y]). \tag{49}$$

Substituting m_x and m_y into (42), the resulting kinematic equations (41), (42) are equivalent to the mechanics-based kinematics derived in [17] and [24].

V. Evaluating Local Elastic Stability

The second-order stability results of Section III can be adapted, as described below, to concentric tube robots to provide a second-order sufficient condition and also a separate necessary condition for stable equilibria. These conditions can be formulated as tests for proving stability and instability, respectively, of candidate configurations as subsequently described in Section V-A.

First, observe that the strengthened Legendre–Clebsch condition is satisfied for all robot configurations since the matrix $C(s) \succ 0$ in (20). Note that $C(s)$ is a diagonal matrix whose diagonal components are the torsional stiffness of each tube, and the sum of x- or y-directional bending stiffnesses of all the tubes. Though there are zero-valued bending stiffnesses for the virtual tubes, the sum is always positive since there exists at least one nonvirtual tube everywhere over the length.

The Jacobi condition must be applied carefully, however, since the standard formulation assumes continuous control candidates and that the integrand and system equation are twice continuously differentiable in x, u, and t [22], [26]. Since robot curvature can be discontinuous with respect to arc length (e.g., piecewise continuous precurvature and at the proximal and distal ends of tubes), this condition is not met. Variations on the standard formulation have been considered. For example, for piecewise control candidates and in the presence of equality/inequality control constraints, a modified Jacobi condition and strengthened Legendre–Clebsch condition are presented in [20] as a sufficient condition for (17). When the control is not subject to any constraints, as in our problem, these conditions reduce to the known form of the classical conditions. Since the strengthened Legendre–Clebsch condition always holds, the Jacobi condition is the only condition required to be sufficient for the second variation to be positive for all nonzero perturbations. In fact, the Jacobi condition is not only sufficient but also necessary for the positive second variation as proven in Appendix A. Consequently, the Jacobi condition is a necessary and sufficient condition for (17) and is thus a sufficient condition for stability.

The derivation of necessary conditions for stability has also been considered when the standard assumptions are not met, e.g., control discontinuity [27]. These conditions are derived under a "normality assumption" on the linearized state equation, as defined in [27], which is not necessarily satisfied for all robot configurations. To match the conditions of concentric tube robots, the following condition is derived in Appendix B.

1) Consider the second variation (19) and the linear system (23)–(26), where $A(s), B(s), C(s)$, and D are given in (20). A necessary condition for stability of the equilibrium point is that this linear system have no solution

(η, v) on $s \in [a, b]$ such that $\eta(c) = 0$ for some c in (a, b) and $\eta(d) \neq 0$ for some d in $[a, c)$.

A. Local Stability Tests for Stable and Unstable Equilibria

The sufficient and necessary conditions given above can be used to classify equilibria as stable and unstable, respectively. Most applications will only require the sufficiency test for stability. The test for instability, which is based on failure to satisfy the necessary condition, is instructive, however, since our numerical examples suggest that configurations not covered by either the sufficient condition or the necessary condition are rare. They are observed to occur only on the boundary between stable and unstable equilibria and correspond to configurations for which higher order tests are needed to evaluate stability.

As presented below, the procedure for performing the local stability tests is based on the transition matrix of a linearized system and is similar in form to the local optimality test of [26]:

1) Solve a backward initial value problem for the differential equation

$$\dot{\Theta} = P\Theta \tag{50}$$

with the following boundary condition:

$$\Theta(b_n) = I \in \mathbb{R}^{(24+2n)\times(24+2n)} \tag{51}$$

where P is defined by (25). We remark that $\dot{x} = f(x, u)$ is the combination of the state equations (28), (36), and (37). $A(s), B(s), C(s)$, and D are given by substituting the Hamiltonian (40) and $h = W$ into (20).

2) Consider a partitioning of Θ into $(12 + n) \times (12 + n)$ submatrices of the form

$$\Theta = \begin{bmatrix} \Theta_{xx} & \Theta_{x\lambda} \\ \Theta_{x\lambda}^T & \Theta_{\lambda\lambda} \end{bmatrix}. \tag{52}$$

Define $X(s) \in \mathbb{R}^{(12+n)\times(12+n)}$ as

$$X(s) = \Theta_{xx}(s) + \Theta_{x\lambda}(s)D \tag{53}$$

where D is given in (20).

3) Then, the sufficiency test for local stability can be stated as: If there is no $c \in [a_n, b_n)$ that satisfies $\det(X(c)) = 0$, the given configuration is a stable equilibrium.
If this is not the case, the next step can be used to test for instability:

4) If there exist $c \in (a_n, b_n)$ and $d \in [a_n, c)$ that satisfy $\det(X(c)) = 0$ and $\det(X(d)) \neq 0$, the given configuration is an unstable equilibrium.

The first and second steps are to compute $X(s)$, the transition matrix for η in the linear system (23), (24), and the third and fourth steps are the tests for stable and unstable equilibria, respectively. The nonsingular transition matrix $X(s)$ over $s \in [a_n, b_n)$ corresponds to the nonexistence of point c conjugate to b_n described in the sufficient condition for stable equilibria, i.e., the Jacobi condition. The test for unstable equilibrium is based on the fact that configurations not satisfying the necessary condition are unstable equilibria since there exists a perturbation with negative second variation as proven in Appendix B.

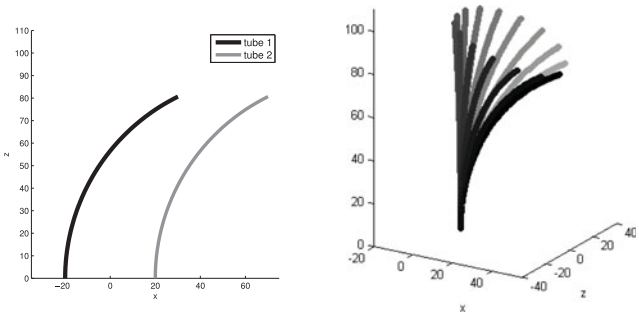

Fig. 4. Variable curvature tube pair. (a) Disassembled tubes. (b) Shape of assembled tubes for various relative base angles.

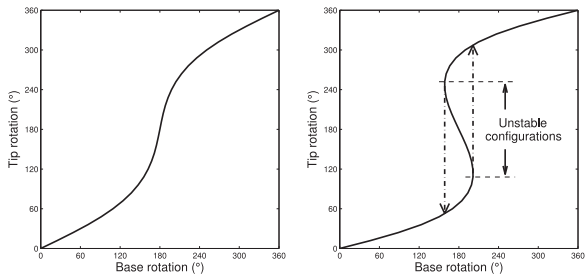

Fig. 5. Relative rotation of tubes at their tips versus their bases. Dashed lines in (b) show jumps between branches of stable solutions. (a) Stable tube pair. (b) Unstable tube pair.

Note that the computations involved in these tests consist of solving a matrix initial value problem and computing determinants during the integration. In numerical implementations, the matrix singularity is detected by observing the sign switching of $\det(X(s))$, or by checking an inequality $|\det X(s)| < \epsilon$ with a small positive margin ϵ. Alternately, $|\det X(s)|$ can be replaced with the condition number of $X(s)$ for robust detection of a nearly singular matrix that is not detected by $|\det X(s)| < \epsilon$.

VI. Numerical Examples

To facilitate understanding of the stability criterion, a series of examples are presented involving constant curvature tube pairs. These examples are used since their unloaded stability has been previously derived [10], [16] and stability can also be presented graphically. In addition, an example demonstrating use of the criterion for stable path planning of a three-tube robot is also presented.

A. Example 1: Stability of an Unloaded Constant-Precurvature Tube Pair

When a pair of tubes of equal precurvature and stiffness are rotated with respect to each other, their mutual curvature varies between the precurvature value and zero (straight) as shown in Fig. 4. The unloaded stability of such tube pairs has been derived previously and can be represented graphically as shown in Fig. 5, which plots relative rotation angle of the tubes at their tip as a function of relative rotation angle at their base

TABLE I
TUBE AND LOAD PARAMETERS FOR EXAMPLES

		Tube 1	Tube 2	
		Section 1	Section 1	Section 2
Example 1	Length (mm)	100	17	100
	Curvature (mm^{-1})	$1/60$	0.0	$1/60$
	Bending Stiffness	1	1	1
	Torsional Stiffness	$1/1.3$	$1/1.3$	$1/1.3$
	a_i (mm)	0	-17	
	b_i (mm)	100	100	
Example 2	Length (mm)	100	17	100
	Curvature (mm^{-1})	$1/79$	0.0	$1/79$
	Bending Stiffness	1	1	1
	Torsional Stiffness	$1/1.3$	$1/1.3$	$1/1.3$
	a_i (mm)	0	-17	
	b_i (mm)	100	100	
	k_{f_e} (mm^{-4})		1.0×10^{-7}	
	k_{F_e} (mm^{-3})		1.0×10^{-5}	
Example 3	Length (mm)	100	17	100
	Curvature (mm^{-1})	$1/60$	0.0	$1/60$
	Bending Stiffness	1	1	1
	Torsional Stiffness	$1/1.3$	$1/1.3$	$1/1.3$
	a_i (mm)	0	-17	
	b_i (mm)	100	100	
	$u(s)$ (mm^{-3})		$-[5.0\ 5.0\ 5.0]^T \times 10^{-7}$	
	U (mm^{-2})		$-[5.0\ 5.0\ 5.0]^T \times 10^{-5}$	
	k_m (mm^{-2})		2.5×10^{-5}	
	k_M (mm^{-1})		2.5×10^{-3}	
	$v(s)$		$[1\ 0\ 0]^T$	
	V		$[1\ 0\ 0]^T$	

Units for load parameters are normalized with respect to bending stiffness units (force·length^2).

[10]. When a tube pair is globally stable, there exists a unique relative rotation angle at the tips of the tubes for each relative rotation angle at the base. This case is depicted in Fig. 5(a).

Configurations can be unstable when multiple tip rotations are associated with the same base rotation. This situation is shown in Fig. 5(b) for configurations with base rotations in the neighborhood of 180°. The stability of a specific solution depends on whether or not perturbations to that solution lead a lower-energy solution. As the tubes are rotated at their base from 0°, they traverse a stable portion of the curve and then jump over the higher energy unstable solutions to the other stable branch.

As a specific example, consider a tube pair with Example 1 parameters given in Table I. This tube pair possesses unstable configurations as shown in Fig. 6(a). The three labeled points correspond to the three possible cases of the stability result by the tests presented in Section V-A. Point 3 corresponds to a stable configuration that satisfies the sufficient condition, while Point 1 is an unstable configuration that fails the necessary condition. Point 2 does not satisfy either of the conditions. In Fig. 5(b), this corresponds to the jump from one stable branch to the other.

B. Example 2: Stability of a Constant Precurvature Tube Pair Subject to Rotation-Invariant Elastic Forces

Now, consider the effect of elastic forces arising, e.g., from contact with tissue, on the stability of a variable curvature tube pair. We would like to understand if tissue contact can destabilize a robot or, alternately, stabilize it. The parameters from Example 2 as given in Table I are used, and as shown in Fig. 7, the

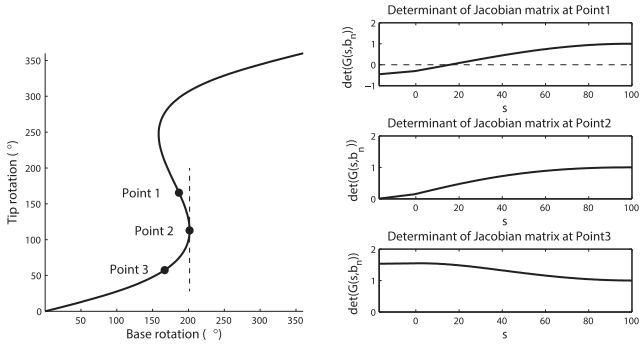

(a) (b)

Fig. 6. Comparison of relative rotation plot with stability criterion. (a) Relative rotation of tubes at their tips versus their base. (b) Determinant of Jacobian computed by (53) versus arc length for three points from (a).

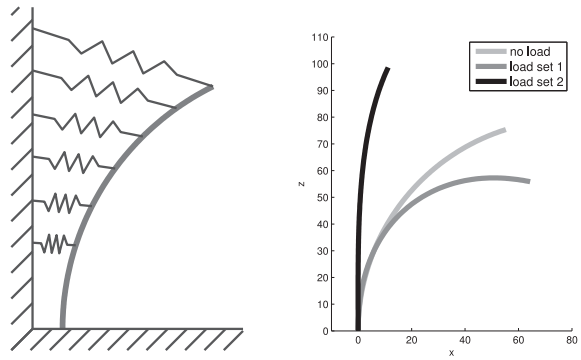

(a) (b)

Fig. 7. Elastic tip and distributed forces applied to a variable curvature tube pair. (a) Load schematic. (b) Shape of robot at maximum curvature for no load, load set 1 and load set 2.

distributed and concentrated elastic forces, $f_e \in \mathbb{R}^3$ and $F_e \in \mathbb{R}^3$, are given by

$$f_e(p(s), s) = k_{f_e}(s)(p(s) - c_{f_e}(s)) \tag{54}$$

$$F_e(p(b_n)) = k_{F_e}(p(b_n) - c_{F_e}) \tag{55}$$

where $c_{f_e}(s) \in \mathbb{R}^3$ is the spring centerline for the distributed elastic force, and $c_{F_e} \in \mathbb{R}^3$ is the spring center of the elastic tip force. $k_{f_e}(s) \in \mathbb{R}$ and $k_{F_e} \in \mathbb{R}$ are the stiffness functions of the distributed elastic force and the stiffness of the elastic tip force, respectively.

To compare our results with those obtained from relative rotation plots as shown above, the forces are defined to be invariant under rotations of the tube set about its base. This is equivalent to fixing $c_{f_e}(s)$ and c_{F_e} in the world frame and performing relative rotation of the tubes such that the robot's plane of curvature remains fixed in the world frame. Note that this is done purely for pedagogical reasons and is not a limitation of the proposed method.

By varying the fixation points of the springs, $c_{f_e}(s)$ and c_{F_e}, it is possible to produce forces that either increase or decrease the curvature of the tube pair [see Fig. 7(b)]. These are given,

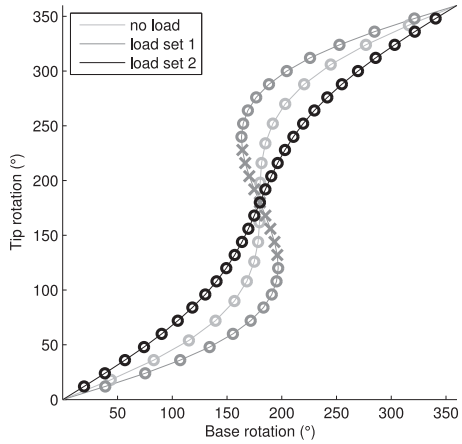

Fig. 8. Relative rotation plots labeled for Example 2. Points on curve labeled stable (o) and unstable (x) using stability criteria.

respectively, by

$$\text{Set 1} \begin{cases} f_e(p(s),s) = -k_{f_e}\left(p(s) - [0\ 0\ (a_n+s)/10]^T\right) \\ F_e(p(b_n),b_n) = -k_{F_e}\left(p(b_n) - [0\ 0\ b_n/10]^T\right) \end{cases} \tag{56}$$

$$\text{Set 2} \begin{cases} f_e(p(s),s) = -k_{f_e}\left(p(s) - [0\ 0\ 2(a_n+s)]^T\right) \\ F_e(p(b_n),b_n) = -k_{F_e}\left(p(b_n) - [0\ 0\ 2b_n]^T\right). \end{cases} \tag{57}$$

The effect of these external loads on stability is compared with the unloaded case in Fig. 8 using the parameter values for Example 2 in Table I. The points labeled "o" in this figure correspond to stable configurations that satisfy the sufficient condition, while the points labeled "x" correspond to unstable configurations that fail to satisfy the necessary condition. Force set 1, which increases the curvature, destabilizes the robot. This can be seen by the shape of the relative rotation curve in Fig. 8. Force set 2, in contrast, reduces robot curvature and, in so doing, stabilizes the robot.

C. Example 3: Stability of a Constant-Precurvature Tube Pair Subject to Rotation-Dependent Loads

This example examines the general case of conservative external loads without the constraint of the preceding example that the loads remain invariant to rotations of the tube set about its base. This general case is depicted in Fig. 9, where it can be seen that the effect of the loads depends not only on the relative angles of the tubes at the robot base, but also on the actual tube base angles. To verify the local stability criteria for this case, a 3-D plot is needed showing tip twist angle as a function of the two base rotation angles.

Let us consider the following potential functions w and W:

$$w = u^T(s)p(s) + \frac{1}{2}k_m \|v(s) - r_z(s)\|^2$$
$$W = U^T p(b_n) + \frac{1}{2}k_M \|V - r_z(b_n)\|^2 \tag{58}$$

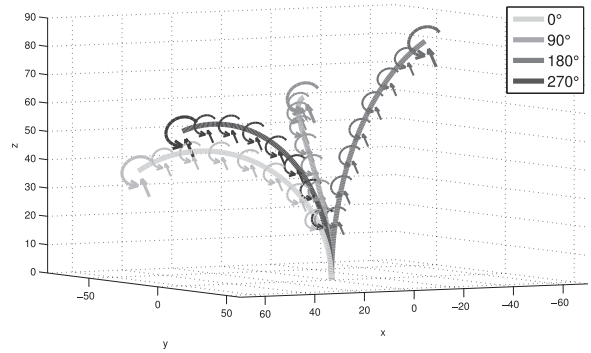

Fig. 9. Effect of constant world-frame loads depends on both base tube angles.

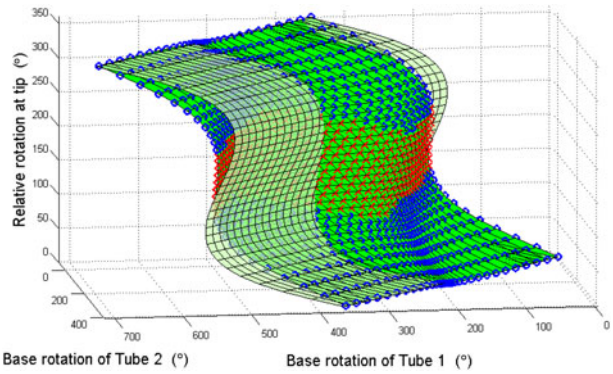

Fig. 10. Stability surfaces for Example 3. Robot without external load corresponds to semitransparent surface. Opaque surface is for externally loaded robot with red X's denoting unstable configurations blue O's denoting stable configurations.

where $u(s), U, v(s), V \in \mathbb{R}^3$ are column vectors such that $\|v(s)\| = \|V\| = 1$, $k_m, k_M \in \mathbb{R}$ are positive scalars, and $r_z(s) \in \mathbb{R}^3$ is the third column of $R(s)$. These potential functions correspond to the distributed force $f(s) = -u(s)$ and the concentrated force $F = -U$, as well as the distributed and concentrated moments that attract the tangent direction of the central axis of the robot to be aligned to $v(s)$ and V, respectively. The general expressions for the distributed and concentrated moment, $m(s)$ and M, can be obtained in the same way as derivations for (48) and (49) by considering infinitesimal displacements in R and corresponding infinitesimal works done by the moments. The resulting $m(s)$ and M expressed in world-frame coordinates are given by

$$m(s) = k_m\left(r_z(s) \times v(s)\right),\ M = k_M\left(r_z(b_n) \times V\right). \tag{59}$$

where $\times$ denotes the cross product.

Fig. 10 depicts relative rotation at the tip as a function of the two base rotation angles. The surfaces with and without external loads are shown. The unloaded surface is semitransparent, while the loaded surface is opaque. The stability tests in Section V-A were used to label the stable and unstable points on the externally loaded surface, while the points on the unloaded surface are unlabeled for clarity. The boundary between the regions of the unstable and stable configurations consists of a curve on which the tangent planes are parallel to the vertical axis. This is

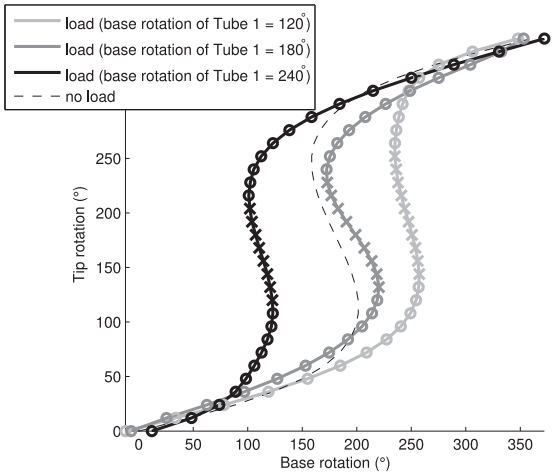

Fig. 11. Relative rotation plots for Example 3 and Tube 1 rotation angles of 120°, 180°, and 240°. Points are labeled stable (o) and unstable (x) using stability criteria.

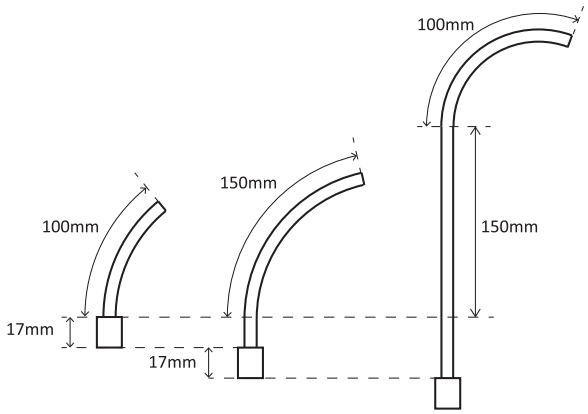

Fig. 12. Tubes comprising robot of Example 4.

consistent with the observation for the preceding 2-D plots that the stability boundary corresponds to points of infinite slope.

Fig. 11 depicts slices through the surfaces of Fig. 10 for Tube 1 rotation angles of 120°, 180°, and 240°. The no-load case appears as a single curve since it is invariant under base rotations of Tube 1. It is observed that the loading can both stabilize and destabilize specific configurations.

D. Example 4: Application to Stable Path Planning

To illustrate the use of our stability criterion, an example of stable path planning using the RRT algorithm is presented here. A three-tube robot design, shown in Fig. 12, is employed using parameters in Table II.

To enable easy interpretation of results, external loads, which have been covered thoroughly in the preceding examples, are not included here. Furthermore, while the three tubes possess a total of six degrees of freedom, only three kinematic inputs are considered so that results can be viewed as a 3-D plot. The kinematic inputs are comprised of rotation of the middle tube as well as translation and rotation of the innermost tube.

TABLE II
EXAMPLE 4 PARAMETERS

	Tube 1	Tube 2		Tube 3	
	Section 1	Section 1	Section 2	Section 1	Section 2
Length (mm)	100	17	150	184	100
Curvature (mm^{-1})	$1/120$	0.0	$1/120$	0.0	$1/60$
Bending Stiffness	1	1	1	0.5	0.5
Torsional Stiffness	$1/1.3$	$1/1.3$	$1/1.3$	$0.5/1.3$	$0.5/1.3$
a_i (mm)	0	-17		$-134 \sim -34$	
b_i (mm)	100	150		$150 \sim 250$	
Initial conf.	$(\theta_2(b_3), \theta_3(b_3), b_3) = (360°, 0°, 170\,\text{mm})$				
Goal conf.	$(\theta_2(b_3), \theta_3(b_3), b_3) = (200°, 200°, 170\,\text{mm})$				

Note that (a_3, b_3) vary with translation length of the innermost tube.

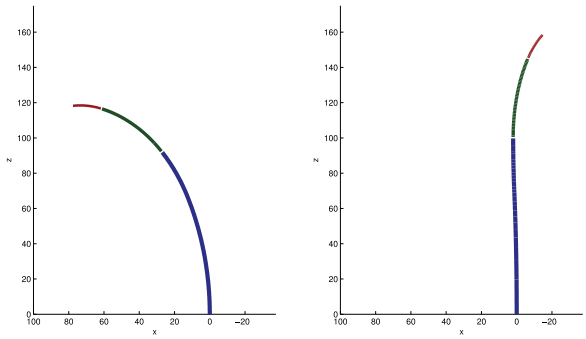

Fig. 13. Initial and goal configurations for stable path planning. (a) Initial configuration. (b) Goal configuration.

Instability can occur in this tube set when the innermost tube is rotated while retracted inside the outer two tubes. To evaluate whether or not path planning using the stability criterion can be used to avoid the unstable configurations, the initial and goal configurations of the robot are defined as shown in Fig. 13 and given in Table II.

Normally, path planning involves solving for a robot path that avoids collisions with obstacles. To plan a stable path, we define here a "collision function" for detecting instability. The final path from RRT after smoothing, however, tends to slide over the surfaces of obstacles. For ensuring stability, this is not a safe approach since it corresponds to operating on the border of instability. We would like to enforce a stability margin, equivalent to a minimum safe distance from obstacles. This is easily accomplished by enforcing an inequality constraint on $\det(X(s))$ from (53):

$$\det(X(s)) > \epsilon \tag{60}$$

where $\epsilon \in \mathbb{R}$ defines the desired stability margin. This approach is used in the collision function defined in Table III.

Fig. 14 depicts the trees and paths generated by the RRT algorithm for stability margin values of $\epsilon = \{0, 0.9\}$. The red curves are the final paths before smoothing, and the green ones are after smoothing. The colored volumes represent the unstable regions. Each color represents the minimum value of $\det(X(s))$ over the length $s \in [a_n, b_n]$. The minimum values of $\det(X(s))$

TABLE III
COLLISION FUNCTION

COLLISION_CHECK$(x^*, \lambda^*, u^*, \epsilon)$	
1	Compute $X(s)$ over $s \in [a_n, b_n]$ for the given stationary solution (x^*, λ^*, u^*), using (53).
2	If $\det(X(s)) > \epsilon$ for $s \in [a_n, b_n]$, return false. Else, return true.

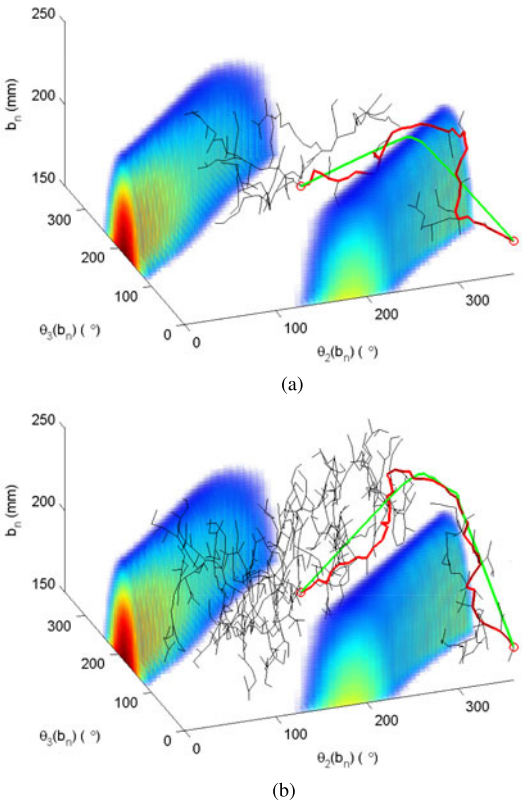

Fig. 14. Configuration space maps showing paths and trees generated by RRT for $\epsilon = \{0, 0.9\}$. Red and green curves are the final paths before and after smoothing, respectively. Colored volumes represent unstable regions. (a) $\epsilon = 0$ (b) $\epsilon = 0.9$

in the red regions are more negative than those in the blue regions. The corresponding motions of the tubes are shown in Fig. 15.

As expected, the direct path between the initial and goal configurations leads through the unstable region. The RRT algorithm has solved for paths in which the innermost tube is first extended and then rotated before being retracted again. Notice in Fig. 14 that, for $\epsilon = 0$, the smoothed green path follows the boundary of the unstable region. When a stability margin is imposed with $\epsilon = 0.9$, however, the smoothed path moves away from the stability boundary to create a condition of robust stability. Physically, increased stability is achieved through greater extension of the innermost tube as shown in Fig. 15.

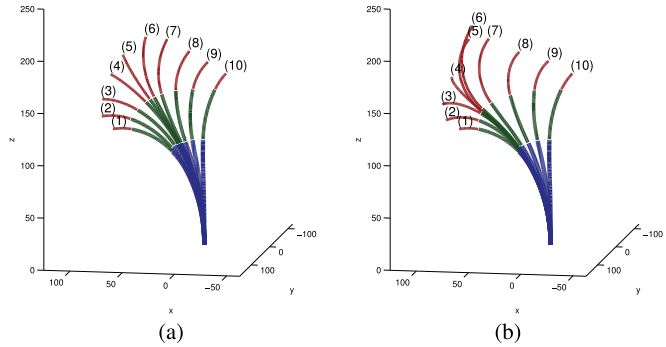

Fig. 15. Final smoothed stable paths for $\epsilon = \{0, 0.9\}$. Numbers indicate sequence of configurations along paths. (a) $\epsilon = 0$. (b) $\epsilon = 0.9$.

VII. CONCLUSION

This paper presents the first general tests for evaluating the stability and instability of concentric tube robot configurations. The tests apply to robots with tubes of arbitrary number, precurvature, and stiffness. They also enable the inclusion of conservative external distributed and tip loads.

The stability criteria are derived by considering the second-order variation of the elastic energy functional when the external loads are conservative. Both a sufficiency condition for evaluating configuration stability and a necessary condition for evaluating instability are presented. They are shown to be numerically consistent with prior stability results.

For the cases considered, the boundary between those solutions satisfying the sufficient condition for stability and those failing to satisfy the necessary condition is comprised of a point in 2-D or a curve in 3-D. While formal evaluation of stability on this boundary would require consideration of higher order terms, practical considerations for robust stability suggest it is advisable to operate away from this boundary.

The kinematic model obtained from the first-order necessary condition requires solving a two-point boundary value problem. Evaluation of the stability tests, however, involves solving only an initial value problem. While demonstrated here in the context of stable path planning, the technique can also be used for generating stable robot designs or, if combined with load sensing, could be used to evaluate safety in real time during robot operation.

APPENDIX A
PROOF OF NECESSITY OF JACOBI CONDITION FOR POSITIVE-DEFINITE SECOND VARIATION

Let us show here that, if the Jacobi condition does not hold, there exists a nonzero admissible perturbation (η, ξ), i.e., the perturbation satisfying the linear system (21), (22), for which the second variation is $\delta^2 J = 0$. Once this is shown, the Jacobi condition is a necessary condition for $\delta^2 J$ in (19) to be always positive for all nonzero admissible perturbation.

Suppose that the Jacobi condition does not hold. Then, there exist a solution (η, v) to the linear system (23), (24) such that $\eta(c) = 0$ for some $c \in [a, b)$. Let (η', v') denote this solution.

Since c exists in $[a, b)$, we can use this c to define $\delta^2 J_1$ and $\delta^2 J_2$ as partitions of $\delta^2 J$, given by

$$\delta^2 J = \delta^2 J_1 + \delta^2 J_2 \tag{61}$$

$$\delta^2 J_1 = \frac{1}{2}\int_a^c \begin{bmatrix} \eta^T & \xi^T \end{bmatrix} \begin{bmatrix} A & B \\ B^T & C \end{bmatrix} \begin{bmatrix} \eta \\ \xi \end{bmatrix} ds \tag{62}$$

$$\delta^2 J_2 = \frac{1}{2}\int_c^b \begin{bmatrix} \eta^T & \xi^T \end{bmatrix} \begin{bmatrix} A & B \\ B^T & C \end{bmatrix} \begin{bmatrix} \eta \\ \xi \end{bmatrix} ds + \frac{1}{2}\eta_f^T D \eta_f . \tag{63}$$

Let us focus on $\delta^2 J_2$ in (63) first. Note that, given the fixed initial point $\eta(c) = 0$, the first-order optimality condition for $\delta^2 J_2$ is equivalent to the linear system (23), (24) and

$$\xi = -C^{-1}\left(B\eta - \frac{\partial f}{\partial u}^T v\right). \tag{64}$$

Since (η', v') is a solution to (23), (24) that satisfies $\eta(c) = 0$, it is a stationary solution of $\delta^2 J_2$, where the optimal control (perturbation) ξ' is given by

$$\xi' = -C^{-1}\left(B\eta' - \frac{\partial f}{\partial u}^T v'\right). \tag{65}$$

Any scaled control $\xi = t\xi'$ and corresponding $(\eta, v) = (t\eta', tv')$ can be easily shown to be a stationary solution of $\delta^2 J_2$ as well, where $t \in \mathbb{R}$, by substituting them into (23), (24) and $\eta(c) = 0$.

Now, consider the following perturbation:

$$\hat{\eta} = \begin{cases} 0, & \text{for } s \in [a, c] \\ \eta', & \text{for } \in (c, b] \end{cases}$$
$$\hat{\xi} = \begin{cases} 0, & \text{for } s \in [a, c] \\ \xi', & \text{for } s \in (c, b]. \end{cases} \tag{66}$$

Note that this is an admissible perturbation since it satisfies the linear system (21), (22). Now, let us show that this perturbation pair makes the second variation zero.

$\delta^2 J_1$ is obviously zero as $(\hat{\eta}, \hat{\xi}) = (0, 0)$ over $s \in [a, c]$. For $\delta^2 J_2$, let us first define a function $q(t) \in \mathbb{R}$ by substituting the stationary solution $(t\eta', t\xi')$ into (63), i.e.,

$$q(t) = \delta^2 J_2(t\eta', t\xi'). \tag{67}$$

Since $\delta^2 J_2$ is stationary for any direction at $(t\eta', t\xi')$, it is also stationary w.r.t t, i.e.,

$$\frac{dq(t)}{dt} = 0. \tag{68}$$

From (68) and the fact that $q(0) = \delta^2 J_2(0, 0) = 0$, $q(t) = 0$ for any $t \in \mathbb{R}$. Thus, $\delta^2 J_2(\hat{\eta}, \hat{\xi}) = q(1) = 0$.

Consequently, the second variation $\delta^2 J = \delta^2 J_1 + \delta^2 J_2$ is zero for a nonzero perturbation $(\hat{\eta}, \hat{\xi})$ when the Jacobi condition does not hold.

APPENDIX B
PROOF OF NECESSITY CONDITION FOR STABLE EQUILIBRIUM

Let us prove the necessary condition of Section V by showing that, if the given condition is not satisfied, there exists an admissible perturbation with $\delta^2 J < 0$.

Suppose that the given condition is not satisfied, i.e., suppose there exists a solution (η, v) to (23), (24) such that $\eta(c) = 0$ for some c in (a, b) and $\eta(d) \neq 0$ for some d in $[a, c)$. In this case, as proven in Appendix A, there exists a nonzero perturbation $(\hat{\eta}, \hat{\xi})$ with $\delta^2 J = 0$, given by (66).

Now, it will be shown that this $(\hat{\eta}, \hat{\xi})$ is not a stationary solution of $\delta^2 J$ in (19). We remark that, at any nonstationary solution, there always exists neighboring admissible pair (η, ξ) toward which the second variation $\delta^2 J$ varies. The second variation may increase along this direction, while decreases along the opposite direction. This yields the existence of an admissible pair (η, ξ) with $\delta^2 J < 0$.

Note that, given the boundary condition $\eta(0) = 0$, the first-order optimality condition for $\delta^2 J$ is given by (23), (24), and

$$\xi = -C^{-1}\left(B\eta - \frac{\partial f}{\partial u}^T v\right). \tag{69}$$

As shown in Appendix A, $(\hat{\eta}, \hat{\xi})$ in (66) satisfies the first-order optimality condition over $s \in [c, b]$. However, continuous backward integration of (23) from c to a yields $\eta(d) \neq 0$ for some d in $[a, c)$. Since $\hat{\eta}(d) = 0$ for any d in $[a, c)$, the perturbation $(\hat{\eta}, \hat{\xi})$ does not satisfy the first-order optimality condition and is thus not a stationary solution.

REFERENCES

[1] J. Burgner *et al.*, "A telerobotic system for transnasal surgery," *IEEE/ASME Trans. Mechatronics*, vol. 19, no. 3, pp. 996–1006, Jun. 2014.

[2] T. Anor *et al.*, "Algorithms for design of continuum robots using the concentric tubes approach: a neurosurgical example," in *Proc. IEEE Int. Conf. Robot. Autom.*, 2011, pp. 667–673.

[3] L. A. Lyons *et al.*, "Motion planning for active cannulas," in *Proc. IEEE/RSJ Int. Conf. Intell. Robots Syst.*, 2009, pp. 801–806.

[4] L. Lyons *et al.*, "Planning active cannula configurations through tubular anatomy," in *Proc. IEEE Int. Conf. Robot. Autom.*, 2010, pp. 2082–2087.

[5] L. G. Torres *et al.*, "Task-oriented design of concentric tube robots using mechanics-based models," in *Proc. IEEE/RSJ Int. Conf. Intell. Robots Syst.*, 2012, pp. 4449–4455.

[6] C. Bedell *et al.*, "Design optimization of concentric tube robots based on task and anatomical constraints," in *Proc. IEEE Int. Conf. Robot. Autom.*, 2011, pp. 398–403.

[7] A. H. Gosline *et al.*, "Percutaneous intracardiac beating-heart surgery using metal MEMS tissue approximation tools," *Int. J. Robot. Res.*, vol. 31, no. 9, pp. 1081–1093, 2012.

[8] N. V. Vasilyev *et al.*, "Percutaneous steerable robotic tool delivery platform and metal MEMS device for tissue manipulation and approximation closure of patent foramen ovale in an animal model," *Circulation: Cardiovascular Interventions*, vol. 6, no. 4, pp. 468–475, 2013.

[9] N. V. Vasilyev *et al.*, "Tissue removal inside the beating heart using a robotically delivered metal MEMS tool," *Int. J. Robot. Res.*, vol. 34, no. 2, pp. 236–247, 2015.

[10] P. E. Dupont *et al.*, "Design and control of concentric-tube robots," *IEEE Trans. Robot.*, vol. 26, no. 2, pp. 209–225, Apr. 2010.

[11] R. Webster *et al.*, "Kinematics and calibration of active cannulas," in *Proc. IEEE Int. Conf. Robot. Autom.*, 2008, pp. 3888–3895.

[12] R. J. Webster *et al.*, "Mechanics of precurved-tube continuum robots," *IEEE Trans. Robot.*, vol. 25, no. 1, pp. 67–78, Feb. 2009.

[13] S. M. LaValle, "Rapidly-exploring random trees: A new tool for path planning," Comput. Sci. Dept., Iowa State Univ., Ames, Tech. Rep. 11, 1998.

[14] C. Bergeles *et al.*, "Concentric tube robot design and optimization based on task and anatomical constraints," *IEEE Trans. Robot.*, vol. 31, no. 1, pp. 67–84, Feb. 2015.
[15] J. Ha *et al.*, "Achieving elastic stability of concentric tube robots through optimization of tube precurvature," in *Proc. IEEE/RSJ Int. Conf. Intell. Robots Syst.*, 2014, pp. 864–870.
[16] R. Xu *et al.*, "Kinematic instability in concentric-tube robots: Modeling and analysis," in *Proc. 5th IEEE RAS & EMBS Int. Conf. Biomed. Robot. Biomechatron.*, 2014, pp. 163–168.
[17] J. Lock *et al.*, "Quasistatic modeling of concentric tube robots with external loads," in *Proc. IEEE/RSJ Int. Conf. Intell. Robots Syst.*, 2010, pp. 2325–2332.
[18] D. C. Rucker *et al.*, "Equilibrium conformations of concentric-tube continuum robots," *Int. J. Robot. Res.*, vol. 29, no. 10, pp. 1263–1280, 2010.
[19] R. L. Bishop, "There is more than one way to frame a curve," *Amer. Math. Monthly*, vol. 82, no. 3, pp. 246–251, Mar. 1975.
[20] D. Orrell and V. Zeidan, "Another jacobi sufficiency criterion for optimal control with smooth constraints," *J. Optim. Theory Appl.*, vol. 58, no. 2, pp. 283–300, 1988.
[21] D. Liberzon, *Calculus of Variations and Optimal Control Theory: A Concise Introduction*. Princeton, NJ, USA: Princeton Univ. Press, 2012.
[22] D. G. Hull, *Optimal Control Theory for Applications*. New York, NY, USA: Springer Science & Business Media, 2013.
[23] J. F. Rosenblueth, "Conjugate journey in optimal control," *Int. Math. Forum*, vol. 2, no. 14, pp. 633–674, 2007.
[24] D. C. Rucker *et al.*, "A geometrically exact model for externally-loaded concentric-tube continuum robots," *IEEE Trans. Robot.*, vol. 26, no. 5, pp. 769–780, Oct. 2010.
[25] F. C. Park and B. J. Martin, "Robot sensor calibration: Solving AX= XB on the Euclidean group," *IEEE Trans. Robot. Autom.*, vol. 10, no. 5, pp. 717–721, Oct. 1994.
[26] J. E. Prussing and S. L. Sandrik, "Second-order necessary conditions and sufficient conditions applied to continuous-thrust trajectories," *J. Guidance, Control, Dyn.*, vol. 28, no. 4, pp. 812–816, 2005.
[27] V. Zeidan and P. Zezza, "Necessary conditions for optimal control problems: Conjugate points," *SIAM J. Control Optim.*, vol. 26, no. 3, pp. 592–608, 1988.

Junhyoung Ha (M'15) received the B.S. and Ph.D. degrees in mechanical engineering from Seoul National University, Seoul, Korea, in 2008 and 2015, respectively.

During the Ph.D. study, he was a Research Assistant for the Robotics Laboratory in the School of Mechanical and Aerospace Engineering, Seoul National University. He is currently with Boston Children's Hospital, Harvard Medical School, Boston, MA, USA. His research interests include medical robotics, continuum robot, control, and optimization.

Frank C. Park (F'13) received the B.S. degree in electrical engineering from the Massachusetts Institute of Technology, Cambridge, MA, USA, in 1985, and the Ph.D. degree in applied mathematics from Harvard University, Cambridge, in 1991.

From 1991 to 1995, he was an Assistant Professor of mechanical and aerospace engineering at the University of California, Irvine. Since 1995, he has been a Professor of mechanical and aerospace engineering at Seoul National University, Seoul, Korea. His research interests include robot mechanics, planning and control, vision and image processing, and related areas of applied mathematics.

Dr. Park has been an IEEE Robotics and Automation Society Distinguished Lecturer and received Best Paper Awards for his work on visual tracking and parallel robot design. He has served on the Editorial Boards of the *Springer Handbook of Robotics*, *Springer Advanced Tracts in Robotics (STAR)*, *Robotica*, and the *ASME Journal of Mechanisms and Robotics*. He has held adjunct faculty positions at the NYU Courant Institute and the Interactive Computing Department at Georgia Tech. He is the Editor-in-Chief of the IEEE TRANSACTIONS ON ROBOTICS and developer of the EDX course Robot Mechanics and Control I, II.

Pierre E. Dupont (M'99–SM'03–F'11) received the B.S., M.S., and Ph.D. degrees in mechanical engineering from Rensselaer Polytechnic Institute, Troy, NY, USA, in 1982, 1984, and 1988, respectively.

From 1988 to 1990, he was a Postdoctoral Fellow with the School of Engineering and Applied Sciences, Harvard University, Cambridge, MA, USA. He was a Professor of mechanical engineering and biomedical engineering with Boston University, Boston, MA. He is currently the Chief of Pediatric Cardiac Bioengineering with Boston Children's Hospital, Harvard Medical School, Boston, where he is involved in developing instrumentation and imaging technology for minimally invasive surgery.